

PNAS PNAS PNAS

<sup>a</sup>Department of Biochemistry, University of Toronto, Toronto, ON, Canada M5S 1A8; <sup>b</sup>Unit for Virus Host-Cell Interactions (UVHCI), Unité Mixte de Internationale (UMI) 3265, Université Joseph Fourier (UJF)-European Molecular Biology Laboratory (EMBL) Grenoble Outstation-Centre National de la Recherche Scientifique (CNRS), 6 rue Jules Horowitz, 38042 Grenoble, France; <sup>c</sup>Institut de Biologie Structurale (IBS) Jean-Pierre Ebel, Unité Mixte de Recherche (UMR) 5075, Commissariat à l'Énergie Atomique (CEA)-CNRS-UJF, 41 rue Jules Horowitz, 38027 Grenoble, France; and <sup>d</sup>Institut Universitaire de France (IUF), 103 Boulevard St. Michel, 75005 Paris, France

BIOCHEMISTRY

438–441 (Fig. 1A), are missing in the final electron density map and are indicated by dotted lines in Fig. 1B.

The RavA monomer has a complex elongated overall structure consisting of three distinct domains (Fig. 1A and B). The N-terminal domain of RavA is the AAA+ module, which is composed of two subdomains: the  $\alpha\beta\alpha$  subdomain (residues 1–192, brown) and the all- $\alpha$  subdomain (residues 226–306, wheat). The  $\alpha\beta\alpha$  subdomain exhibits a Rossmann-type fold commonly found in nucleotide binding proteins. It consists of a central  $\beta$ -sheet with five parallel  $\beta$ -strands, ordered as 51432, sandwiched between seven  $\alpha$ -helices. The all- $\alpha$  subdomain consists of four antiparallel  $\alpha$ -helices. The  $\alpha\beta\alpha$  subdomain and the all- $\alpha$  subdomain are linked by a 32-residue helical segment (residues 193–225, green). The relative arrangement of the subdomains is similar to that found in Mg chelatases (discussed below).

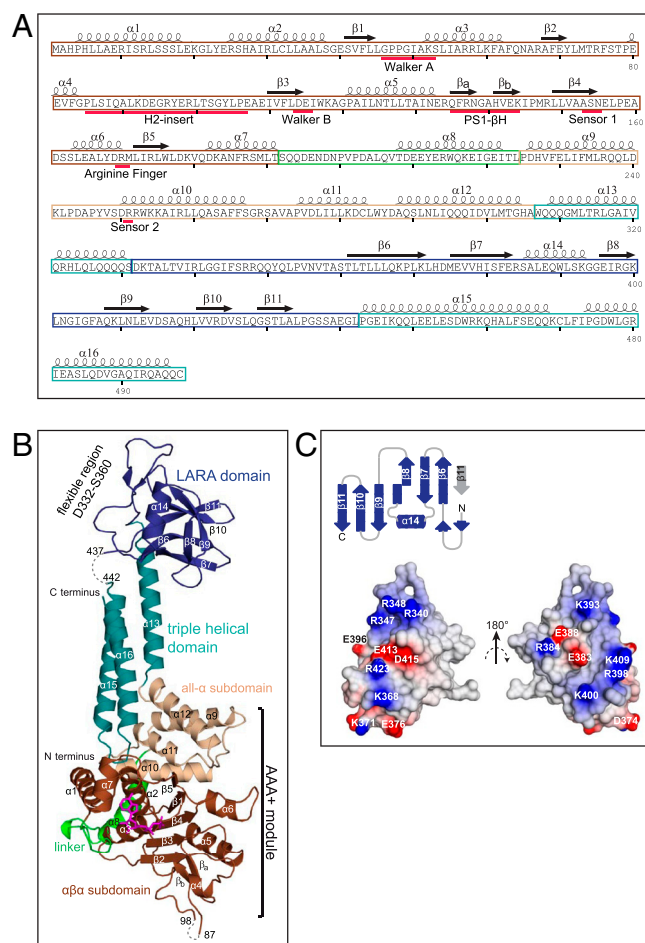


**Fig. 1.** Overall view of RavA protomer structure. (A) Sequence of *E. coli* RavA showing secondary structure and conserved motifs. (B) X-ray structure of RavA protomer.  $\alpha\beta\alpha$  subdomain is shown in brown, all- $\alpha$  subdomain is shown in wheat, the linker between the two subdomains is shown in green, triple-helical bundle domain is shown in blue, the LARA domain is shown in dark blue, and bound ADP is shown in violet. The  $\alpha$ -helices and  $\beta$ -strands are labeled sequentially except for  $\beta_a$  and  $\beta_b$  of the Pre-Sensor 1  $\beta$ -Hairpin insertion. Residues 88–97 and 438–441 were not observed in the X-ray structure and are indicated by a dashed line. The figure was generated using PYMOL. (C) Shown is a topological diagram of the LARA domain drawn using TopDraw (25) and its electrostatic surface potential calculated using Delphi (26). Colors are according to the calculated electrostatic surface potential and range from red (potential of  $-5$  kT) to blue ( $+5$  kT). The hydrophobic core of the domain is made by the side chains of hydrophobic residues from each of the  $\beta$ -strands ( $\beta 1$ : L362, L364, L366, L372;  $\beta 2$ : V377, I380, F382;  $\beta 3$ : I397, L401;  $\beta 4$ : L410, L412;  $\beta 5$ : L420, V422;  $\beta 6$ : L432) as well as residues L387, W390 and L391 from the  $\alpha 14$  helix.

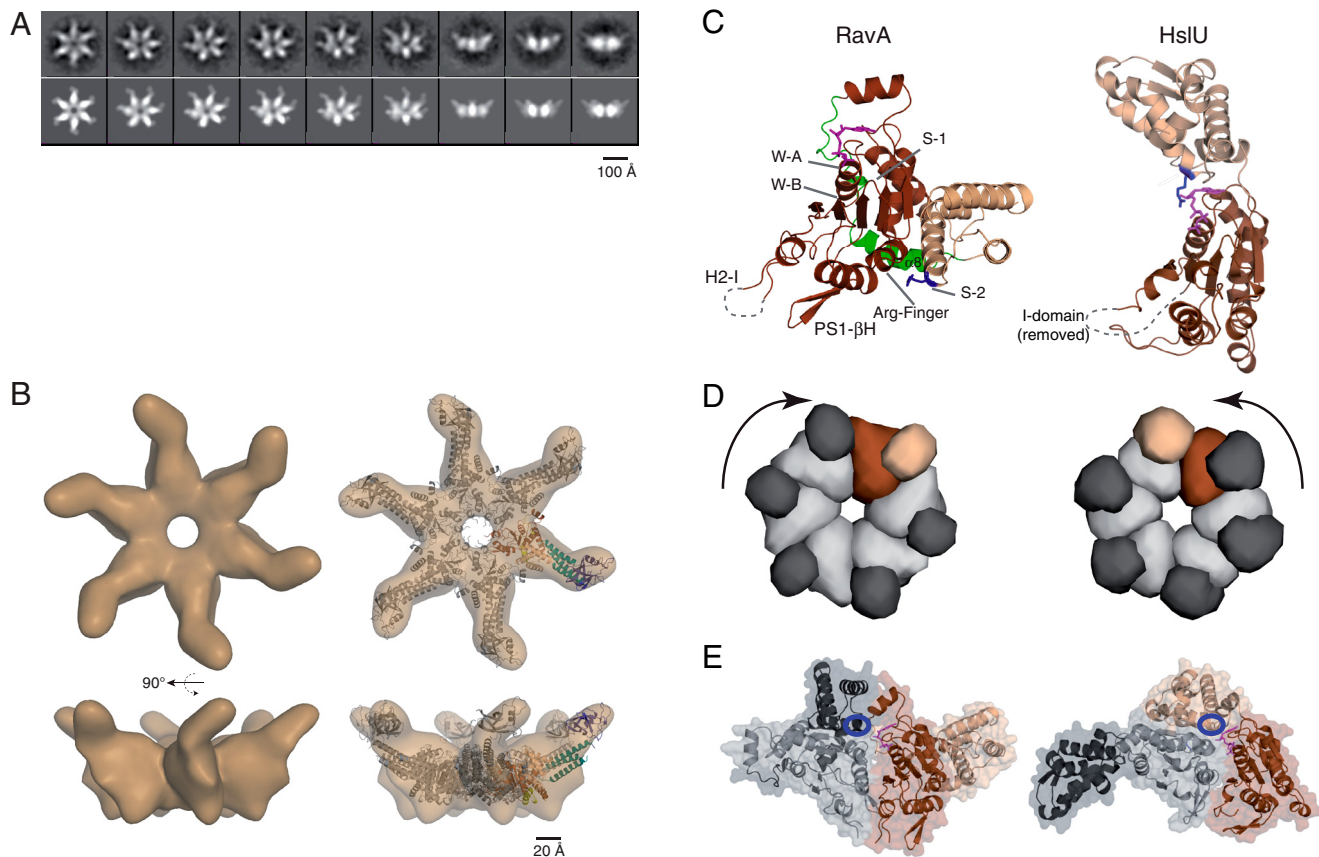
The second domain is a discontinuous triple-helical domain formed by helices  $\alpha 13$ ,  $\alpha 15$ , and  $\alpha 16$  (residues 307–330 and 442–497, light blue). This domain has a rigid structure stabilized by hydrophobic interactions localized at the interface between the three helices. The third domain (residues 331–437, dark blue), which we have named the LARA domain (for reasons described below), is a protuberance between helices  $\alpha 13$  and  $\alpha 15$  of the triple-helical domain. As shown in Fig. 1B and C, the LARA domain forms a compact antiparallel  $\beta$ -barrel-like structure consisting of six  $\beta$ -strands ( $\beta 6$ – $\beta 11$ ) and one  $\alpha$ -helix ( $\alpha 14$ ). The LARA domain also includes an N-terminal flexible region (residues D332–S360). The domain is very basic (pI of 9.6) resulting from a highly positively charged surface formed by residues R340, R347, R348, R398, K400, K409, and R423 (Fig. 1C). We performed an extensive search for structures similar to that of the LARA domain in the Protein Data Bank using secondary-structure matching (SSM) (13) and Dali (14), but no such structures were found. Hence, we conclude that the *E. coli* RavA LARA domain adopts a unique fold.

The sequence conservation at the C terminus of RavA spanning the triple-helical and LARA domains diverges quite quickly, although, according to secondary-structure prediction, all organisms containing RavA protein with a LARA domain also have a triple-helical domain. It was surprising to find that a phenylalanine (F472), located at the turn between helices  $\alpha 15$  and  $\alpha 16$  of the triple-helical domain, is absolutely conserved (Fig. S14). This phenylalanine makes hydrophobic contacts with the AAA+ module and, hence, anchors the triple-helical bundle to the AAA+ module (Fig. S1B and C). F472 might serve to transmit the nucleotide-dependent conformational changes in the AAA+ domain to the C-terminal triple-helical and LARA domains of RavA.

**RavA Hexameric Assembly.** Although RavA and many other AAA+ ATPases crystallize as monomers, their functional form is well known to be an oligomeric ring structure. Previous work in our laboratory provided first evidence for a hexameric assembly of RavA induced by ATP, ADP, or 5'-adenylyl- $\beta$ , $\gamma$ -imidodiphosphate (AMPPNP) binding (12). Here we present a 3D structure of the RavA hexamer formed in the presence of ADP obtained by negative staining electron microscopy (EM) and image analysis.

Similar to other AAA+ protein structures, hexameric RavA-ADP is characterized by a ring-shaped core surrounding a central pore. Some representative class averages, as well as corresponding projections of the 3D structure at similar orientations, are shown in Fig. 2A. The distinctive feature of the class averages is the relatively weak density of the LARA domain, which necessitated a good alignment in order to be properly visualized (see *Materials and Methods* for details). The RavA hexameric ring forms a rather unique flower-like structure and is found to be about 220 Å in diameter and of 80-Å thickness, whereas the diameter of the central channel is about 25 Å. The 3D reconstruction possesses a prominent handedness, visible in the core AAA+ part and notably accentuated by the protrusions. An atomic model of the hexamer was then generated by docking the crystal structure of the monomer into the EM density of the hexamer and adjustment of the resulting intersubunit contacts based on a homology model generated from the hexameric crystal structure of HslU [PDB ID code 1DO0 (15)] (see *Materials and Methods* and Fig. S2 for details). The final EM reconstruction and the resulting atomic model of the RavA-ADP hexamer are shown in Fig. 2B.

**The Organization of the AAA+ Motor Subdomains.** In their classification of AAA+ proteins, Aravind and coworkers grouped RavA within the helix 2 insert clade (8). Members of this family are found to have (i) an insert within helix 2 of the conserved ASCE (refers to Additional Strand, Catalytic E) division P-loop ATPase core, (ii) a  $\beta$ -hairpin N terminal to Sensor 1, as well as, (iii) a long helical seg-



whereas the subunits in HslU are organized counterclockwise (Fig. 2D).

It should be noted that, in the RavA structure, the all- $\alpha$  and  $\alpha\beta$  subdomains from the same monomer make extensive interactions. The buried surface area between these two subdomains is much larger in the case of RavA (2,797 Å<sup>2</sup>) than for HslU monomer (1,084 Å<sup>2</sup>) (Fig. 2E). As a result, in the HslU hexamer, the all- $\alpha$  subdomain makes more extensive interactions with the  $\alpha\beta$  subdomain of the neighboring protomer (2,930 Å<sup>2</sup>) than in the RavA hexamer (754 Å<sup>2</sup>).

Even with these major differences in the assembly of the subunits, the overall structures of the RavA and HslU AAA+ hexamers remain similar with a high conservation in the organization of the ATP-binding site. Fig. S4 shows the localization of the nucleotide between two subunits of the RavA and HslU hexamers. In both cases, the nucleotide makes contact with three subdomains. For HslU, the nucleotide is sandwiched between the  $\alpha\beta$  and the all- $\alpha$  subdomains of the same subunit and faces the  $\alpha\beta$  subdomain of the left neighboring subunit, whereas the nucleotide in RavA contacts the  $\alpha\beta$  subdomain of one subunit and faces the all- $\alpha$  and the  $\alpha\beta$  subdomains of the left neighboring subunit.

**The LARA Domain Mediates RavA-LdcI Interactions.** Previous work in our laboratory has shown that RavA interacts with LdcI, an inducible lysine decarboxylase enzyme, forming an unusual cage-like complex of about 3.3 MDa consisting of two LdcI (81 kDa) decamers and up to five RavA (56 kDa) hexamers (Fig. 3A) (12). We further confirmed this interaction in this study. The pull-down of RavA from an *E. coli* strain in which a Sequential Peptide Affinity (SPA) tag (22) was fused at the 3' end of the endogenous *ravA* gene, also pulled down LdcI as previously observed (12). Analysis of the complex by size exclusion chromatography showed that the majority of RavA was part of a 3.3-MDa complex with LdcI (Fig. S5A), which corresponds to the mass of the complex shown in Fig. 3A. LdcI migrated as a complex with RavA but also as uncomplexed decamers as well. In another experiment, analysis of the interaction between purified RavA and LdcI proteins by sedimentation velocity analytical ultracentrifugation revealed the presence of 0.8-, 2.7-, and 6.0-MDa complexes (Fig. S5B). These complexes would correspond to LdcI decamer alone, the RavA-LdcI cage-like complex of Fig. 3A, and a dimer of the cage-like complex, respectively.

Docking of RavA hexameric model of Fig. 2B and LdcI decameric crystal structure that we recently determined into the EM envelope suggested that the LARA domain of RavA might interact with LdcI (Fig. 3A and Fig. S6A). To determine the validity of the docking model, a RavA construct was made in which the LARA domain was deleted and was termed RavA $\Delta$ LARA (consisting of residues Met1–Ala335 and Leu434–Cys498). An isolated LARA domain construct was also generated (residues Gln329–Glu440). Circular dichroism analysis showed that both proteins have the expected secondary-structure content. Furthermore, RavA $\Delta$ LARA formed a hexameric complex in the presence of ATP (Fig. S6B), and its ATPase activity was similar to that of WT RavA (Fig. S6B, Inset). The interaction of LdcI with RavA and its different constructs was then assessed by surface plasmon resonance (SPR) using the Biacore system. In these experiments, LdcI was immobilized on the chip. The SPR experiments clearly showed that, although WT RavA and LARA domain do interact with LdcI (Fig. 3B), RavA $\Delta$ LARA does not bind to LdcI (Fig. 3C). In the absence of nucleotide, WT RavA bound LdcI with an apparent binding constant of 0.56  $\mu$ M (Fig. 3B). In the presence of ATP, the binding curve was best fit using two independent binding sites with apparent binding constants of 0.018  $\mu$ M and 1.22  $\mu$ M (Fig. 3B). This might indicate that the proper hexamerization of RavA, which is attained in the presence of ATP, allows for two RavA “legs” to bind the LdcI decamer at two different sites as suggested by the docking analysis of Fig. 3A and Fig. S6A. How-

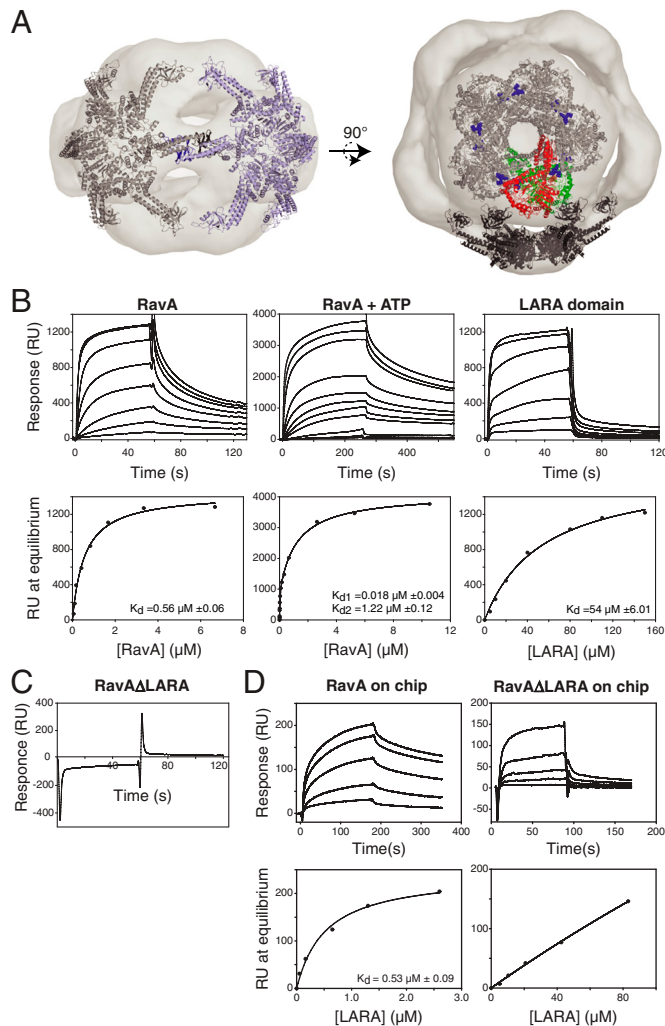


**Fig. 3.** The LARA domain mediates RavA-LdcI and RavA-RavA interactions. (A) Fit of the RavA hexameric model and LdcI decamer into the EM envelope of the LdcI-RavA complex (12) viewed from the side (Left) and the top (Right). One LdcI dimer is colored in red (the upper monomer) and green (the lower monomer). ppGpp bound to LdcI is drawn as blue spheres. (B) Biacore sensorgrams and equilibrium binding curves showing the interaction between LdcI (on chip) and WT RavA in the absence of nucleotide (Left), or WT RavA in the presence of ATP (Middle), or the LARA domain (Right). (C) Biacore sensorgram showing the lack of interaction between LdcI (on chip) and RavA $\Delta$ LARA at 15  $\mu$ M. (D) Biacore sensorgrams and equilibrium binding curves showing the interaction between WT RavA and LARA domain (Left) and the very weak interaction between RavA $\Delta$ LARA and LARA domain (Right).

ever, it should be noted that, because of the experimental setup, the full complex shown in Fig. 3A, in which RavA hexamers can bridge two LdcI decamers, is unlikely to form under the conditions of the SPR experiments because LdcI is cross-linked to the chip. The isolated LARA domain is also able to bind LdcI albeit with a lower apparent  $K_d$  of 54  $\mu$ M (Fig. 3B). Hence, these observations strongly suggest that the LARA domain is the RavA domain required for LdcI interaction, hence the acronym LARA: LdcI associating domain of RavA.

Bioinformatic analysis provided further support for the finding that the LARA domain mediates the interaction of RavA with LdcI. In 47 representative bacterial strains that contained RavA based on BLAST searches (23), we asked whether these strains also contain LdcI. As mentioned earlier, the C-terminal fragment of RavA including the triple-helical bundle and LARA domain is not well conserved. Hence, the presence of the LARA domain in RavA across the different strains was assessed using JPred sec-

ondary structure prediction program (24). It was interesting to find that RavA in all strains containing LdcI has a LARA domain, whereas strains that do not have LdcI contain RavA that has or does not have the LARA domain (Fig. S6C). The LARA domain in these strains might have other functions or the domain will eventually degenerate.

**The LARA Domain Mediates RavA-RavA Interactions.** The docking shown in Fig. 3A suggests that the LARA domain might also mediate RavA-RavA interactions within the RavA-LdcI cage-like complex by interacting with the triple-helical domain and/or the LARA domain of the neighboring RavA (Fig. S6A). SPR experiments were carried out in which RavA or RavA $\Delta$ LARA is immobilized on the chip and the LARA domain is titrated. The results indicate that the LARA domain can bind to RavA with an apparent  $K_d$  of about 0.5  $\mu$ M (Fig. 3D). This interaction is drastically reduced when the binding experiment is performed between RavA $\Delta$ LARA and the LARA domain (Fig. 3D), suggesting that the LARA domain plays an important role in RavA-RavA interactions within the RavA-LdcI cage-like complex.

**RavA Antagonizes the Inhibitory Effect of ppGpp on LdcI Activity.** The LdcI crystal structure revealed the presence of a binding site for the bacterial alarmone guanosine tetraphosphate (ppGpp) at the interface between two protomers in the pentameric ring (Fig. 3A). Biochemical assays showed that ppGpp binding to LdcI results in drastic inhibition of the LdcI activity of approximately 10-fold at pH values greater than 5. The docking shown in Fig. 3A suggests that the LARA domain of RavA might bind at a site in LdcI that could affect ppGpp binding to the decarboxylase.

The activity of the decarboxylase was measured in the presence and absence of RavA and ppGpp using an isothermal titration calorimetry (ITC) approach. Initially, we ensured that the presence of GTP, GDP, ppGpp, and pppGpp does not affect RavA ATPase activity (Fig. 4A). When the RavA-LdcI complex is preformed, LdcI activity is not significantly changed consistent with

our prior observations (12). However, when ppGpp is added to the preformed RavA-LdcI complex, the presence of RavA reduces the inhibitory effect of ppGpp on LdcI by about 40% under the conditions of the experiment (Fig. 4B). Moreover, the RavA- $\Delta$ LARA truncation mutant is not able to reduce the inhibitory effect of ppGpp on LdcI activity, which is consistent with our results showing that the LARA domain is responsible for the RavA-LdcI interaction. When LdcI is preincubated with ppGpp and then RavA is added, RavA is not able to reduce the inhibition of LdcI by the alarmone (Fig. 4C). Hence, RavA either blocks the access to the ppGpp binding site in LdcI or RavA induces a local conformational change in LdcI that reduces its ppGpp binding affinity. Alternatively, ppGpp might cause a conformational change in LdcI to reduce RavA binding to the decarboxylase.

It should be pointed out that the effect of RavA on LdcI inhibition by ppGpp is probably underestimated because these experiments were done at low concentrations of  $MgCl_2$ . Under such conditions, RavA has low ATPase activity; addition of higher concentrations of  $MgCl_2$  lead to the precipitation of ppGpp by  $Mg^{2+}$ .

To further validate our in vitro results and to determine if the modulation of ppGpp binding to LdcI by RavA can be observed in vivo, the activity of LdcI was tested in different strains undergoing a stringent response. Four strains were used:  $\Delta cadBA$ , WT + *ravA*, WT + *ravA* $\Delta$ LARA, and WT + *ravA*(K52Q). The last three strains overexpress *RavA*, *RavA* $\Delta$ LARA, and *RavA*(K52Q) proteins by IPTG induction (refer to *Materials and Methods*). *RavA*(K52Q) is ATPase deficient because the conserved Walker A K52 is mutated to Q (Fig. 1A). Endogenous *RavA* is expressed at low levels and is induced only in the stationary phase (12). Cells were grown to log phase in defined rich media buffered at pH 5, and, when the  $OD_{600}$  of each strain was approximately 0.2, proteins were induced with 1 mM IPTG for 1 h. Cells were then shifted to minimal media weakly buffered at pH 5 containing no amino acids to induce ppGpp production, and supplemented with 30 mM lysine to follow the LdcI activity by monitoring pH change of the media; no cell growth occurs during

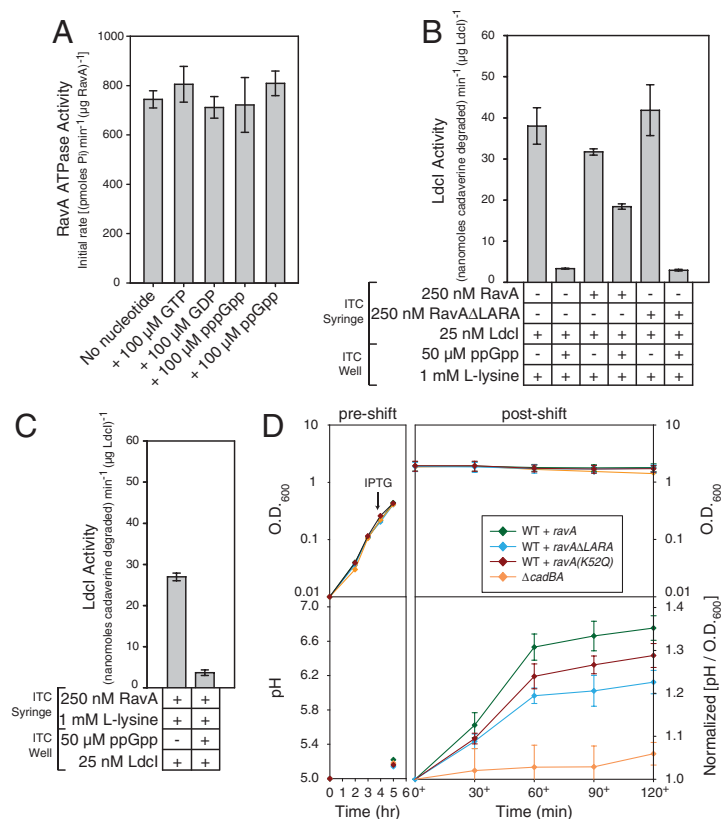


**Fig. 4.** RavA binding to LdcI antagonizes the inhibitory effect of ppGpp on LdcI activity. (A) The ATPase activity of RavA measured by ITC in the presence of different nucleotides. Error bars represent the standard deviation of the average of three experiments. (B) LdcI activity measured by ITC in the presence of RavA or RavA $\Delta$ LARA and/or ppGpp. Note that the concentrations of proteins, substrate, and inhibitor are the final concentrations after mixing. In this panel, the RavA-LdcI complex is preformed in the syringe before adding ppGpp. (C) LdcI activity measured by ITC. In this experiment, LdcI-ppGpp complex is preformed in the well before adding RavA. (D) The effect of RavA overexpression on LdcI activity in the cell.  $\Delta cadBA$  knockout strains and WT cells overexpressing RavA, RavA $\Delta$ LARA, or RavA(K52Q) were grown to log phase in defined rich media buffered at pH 5. RavA, RavA $\Delta$ LARA, or RavA(K52Q) were induced and cells were then shifted to minimal media weakly buffered at pH 5 containing no amino acids to induce ppGpp production and supplemented with 30 mM lysine. The  $OD_{600}$  of the cells is shown (Top); the pH of the culture media is shown (Bottom Left). (Bottom Right) The increase in pH/ $OD_{600}$  normalized to the value at 0+ (right after shift). Each time point is the result of at least three replicates. Error bars represent the standard deviations of the measurements.

this time (Fig. 4D and Fig. S7). Consistent with the in vitro results, WT + *ravA* strain increased the pH of the media at a higher rate than the WT + *ravA*ΔLARA strain, whereas no significant pH change was observed for the Δ*cadBA* cells (Fig. 4D). Hence, the formation of the RavA-LdcI complex reduced the inhibitory effect of the alarmone on LdcI, allowing the cells to better respond to low acidity. On the other hand, RavAΔLARA cannot form a complex with LdcI (Fig. 3D) and, hence, LdcI should still be inhibited by ppGpp resulting in a lower rate of pH increase, as observed (Fig. 4D). The strain overexpressing RavA(K52Q) mutant increased pH faster than the strain overexpressing RavA-ΔLARA, but not as well as the strain overexpressing WT RavA (Fig. 4D), indicating that the binding of RavA to LdcI is not enough to modulate alarmone binding to the decarboxylase, but that the ATPase activity of RavA is also needed.

## Discussion

The organization of the AAA+ module of RavA as revealed by the X-ray structure of the protein (Figs. 1B and 2C) explicitly demonstrates that the protein is closely related to the family of Mg chelataes. We had previously found that RavA and LdcI interact tightly to form an unusual cage-like structure (12). Having the X-ray structure and the EM reconstruction of RavA (this study), as well as the X-ray structure of LdcI and the negative staining EM reconstruction of the RavA-LdcI complex (12), allowed us to gain important insights into the design principles of this cage that is formed by the interaction of a fivefold symmetric oligomer of LdcI with a sixfold symmetric oligomer of RavA (Fig. 3A). The RavA hexamer displays six “legs,” which are spanning the triple-helical domain and the LARA domain. Two of the legs interact with an LdcI dimer at the top of the complex, and two other legs show the same set of interactions with an LdcI dimer at the bottom of the complex. These interactions seem to be mainly mediated by the LARA domain. The two remaining legs of RavA are interacting with a neighboring RavA leg on the left and on the right (Fig. 3A and Fig. S6A). The RavA-RavA leg-leg interactions seem to involve the triple-helical domain, as well as the LARA domain (Fig. 3A). Hence, the construction of the RavA leg makes all these interactions possible. The LARA domain exhibits a unique fold and, based on the bioinformatic analysis of Fig. S6C, seems to be optimally evolved to mediate the interaction of RavA with LdcI.

The RavA-LdcI cage-like structure might have multiple functions in the cell yet to be elucidated; however, one consequence we found here for the formation of the RavA-LdcI complex is the reduction of the inhibitory effect of ppGpp on LdcI activity. When cells are undergoing acid stress and LdcI is induced to about 2,000 decamers per cell, nutrient limitation will result in the production of the alarmone. Because we estimate that there are about 50–100 RavA hexamers per cell in the stationary phase (12), only a small population of LdcI molecules is expected to be in complex with RavA. This population of LdcI will not be strongly inhibited by ppGpp, allowing the cells to continue to respond to acid stress at the risk of depleting lysine amounts. It is interesting to note that RavA and ppGpp have similar binding constants to LdcI:  $K_d$  of 0.02–1  $\mu$ M for RavA-LdcI interaction (Fig. 3B) and  $K_d$  of 0.01–0.7  $\mu$ M for LdcI-ppGpp interaction. The binding of RavA to apo-LdcI does not affect LdcI activity to any significant extent (Fig. 4B and ref. 12). Hence, there is a fine-tuning of LdcI activity by ppGpp and RavA, which is required for the cells to respond to acid stress, as well as to prevent the depletion of their amino acids. This fine-tuning probably involves other factors and proteins and also occurs for other amino acid decarboxylases involved in the bacterial acid stress response.

## Materials and Methods

Details of cloning, protein expression and purification, RavA ATPase assay, SPR measurements, LdcI enzyme kinetics measurements using ITC, sedimentation velocity analytical ultracentrifugation, pull-down experiments, media shift assays, X-ray crystallography, and electron microscopy are provided in *SI Text*.

**ACKNOWLEDGMENTS.** We thank Dr. Elisabeth Tillier (University of Toronto) for her help with the bioinformatic analysis shown in Fig. S6C. We also thank several members of UVHCI: Dr. Rob Ruigrok for his support, Dr. Hassan Belrhali for help with data collection and phasing, Dr. Monika Spano, Dr. Nicolas Tarbouriech, and Dr. Thibaut Cr  pin for help with protein crystallization. M.E.B. is the recipient of a fellowship from the Canadian Institutes of Health Research (CIHR) Strategic Training Program in Protein Folding and Interaction Dynamics: Principles and Diseases. U.K. is the recipient of a National Sciences and Engineering Research Council of Canada (NSERC) Postgraduate Scholarship, a Canadian Institutes of Health Research Strategic Training Program in the Structural Biology of Membrane Proteins Linked to Disease, and a University of Toronto Open Fellowship. B.Z. is the recipient of NSERC Alexander Graham Bell Canada Graduate Scholarship. M.Y. is the recipient of Life Sciences Award from the University of Toronto. This work was supported by a grant from CIHR (MOP-67210) (to W.A.H.).

- Kunau WH, et al. (1993) Two complementary approaches to study peroxisome biogenesis in *Saccharomyces cerevisiae*: Forward and reversed genetics. *Biochimie* 75:209–224.
- Confalonieri F, Duguet M (1995) A 200-amino acid ATPase module in search of a basic function. *Bioessays* 17:639–650.
- Ogura T, Wilkinson AJ (2001) AAA+ superfamily ATPases: Common structure—diverse function. *Genes Cells* 6:575–597.
- Leipe DD, Koonin EV, Aravind L (2003) Evolution and classification of P-loop kinases and related proteins. *J Mol Biol* 333:781–815.
- Ammelburg M, Frickey T, Lupas AN (2006) Classification of AAA+ proteins. *J Struct Biol* 156(1):2–11.
- Snider J, Thibault G, Houry WA (2008) The AAA+ superfamily of functionally diverse proteins. *Genome Biol* 9:216.
- Neuwald AF, Aravind L, Spouge JL, Koonin EV (1999) AAA+: A class of chaperone-like ATPases associated with the assembly, operation, and disassembly of protein complexes. *Genome Res* 9:27–43.
- Iyer LM, Leipe DD, Koonin EV, Aravind L (2004) Evolutionary history and higher order classification of AAA+ ATPases. *J Struct Biol* 146:11–31.
- Ogura T, Whiteheart SW, Wilkinson AJ (2004) Conserved arginine residues implicated in ATP hydrolysis, nucleotide-sensing, and inter-subunit interactions in AAA and AAA+ ATPases. *J Struct Biol* 146:106–112.
- Hanson PI, Whiteheart SW (2005) AAA+ proteins: Have engine, will work. *Nat Rev Mol Cell Biol* 6:519–529.
- Snider J, Houry WA (2006) MoxR AAA+ ATPases: A novel family of molecular chaperones? *J Struct Biol* 156:200–209.
- Snider J, et al. (2006) Formation of a distinctive complex between the inducible bacterial lysine decarboxylase and a novel AAA+ ATPase. *J Biol Chem* 281:1532–1546.
- Krissinel E, Henrick K (2004) Secondary-structure matching (SSM), a new tool for fast protein structure alignment in three dimensions. *Acta Crystallogr D* 60:2256–2268.
- Holm L, Kaariainen S, Rosenstrom P, Schenkel A (2008) Searching protein structure databases with DALI Lite v.3. *Bioinformatics* 24:2780–2781.
- Bochtler M, et al. (2000) The structures of HslU and the ATP-dependent protease HslU-HslV. *Nature* 403:800–805.
- Fodje MN, et al. (2001) Interplay between an AAA module and an integrin I domain may regulate the function of magnesium chelatase. *J Mol Biol* 311:111–122.
- Han YW, et al. (2001) A unique beta-hairpin protruding from AAA+ ATPase domain of RuvB motor protein is involved in the interaction with RuvA DNA recognition protein for branch migration of Holliday junctions. *J Biol Chem* 276:35024–35028.
- Lee SY, et al. (2003) Regulation of the transcriptional activator NtrC1: Structural studies of the regulatory and AAA+ ATPase domains. *Genes Dev* 17:2552–2563.
- Shen J, Gai D, Patrick A, Greenleaf WB, Chen XS (2005) The roles of the residues on the channel beta-hairpin and loop structures of simian virus 40 hexameric helicase. *Proc Natl Acad Sci USA* 102:11248–11253.
- Jenkinson ER, Chong JP (2006) Minichromosome maintenance helicase activity is controlled by N- and C-terminal motifs and requires the ATPase domain helix-2 insert. *Proc Natl Acad Sci USA* 103:7613–7618.
- Erzberger JP, Berger JM (2006) Evolutionary relationships and structural mechanisms of AAA+ proteins. *Annu Rev Biophys Biomol Struct* 35:93–114.
- Babu M, et al. (2009) Sequential peptide affinity purification system for the systematic isolation and identification of protein complexes from *Escherichia coli*. *Methods Mol Biol* 564:373–400.
- Altschul SF, et al. (1997) Gapped BLAST and PSI-BLAST: A new generation of protein database search programs. *Nucleic Acids Res* 25:3389–3402.
- Cole C, Barber JD, Barton GJ (2008) The Jpred 3 secondary structure prediction server. *Nucleic Acids Res* 36:W197–201.
- Bond CS (2003) TopDraw: A sketchpad for protein structure topology cartoons. *Bioinformatics* 19:311–312.
- Rocchia W, et al. (2002) Rapid grid-based construction of the molecular surface and the use of induced surface charge to calculate reaction field energies: Applications to the molecular systems and geometric objects. *J Comput Chem* 23:128–137.

# Supporting Information

El Bakkouri et al. 10.1073/pnas.1009092107

## SI Materials and Methods

**Cloning.** The LARA domain (Gln329–Glu440) was PCR amplified from the p11-RavA plasmid (1). The PCR product was digested with *NdeI* and *BamHI* (NEB) and ligated into an empty p11 vector to produce p11-LARA. The resulting construct has an N-terminal His<sub>6</sub>-tag followed by a tobacco etch virus (TEV) cut site that leaves the three residues GHM at the N terminus of the construct after TEV cleavage. The RavAΔLARA (Met1–Ala335 and Leu434–Cys498) was constructed by PCR amplification of two fragments of the *ravA* gene that bear a *BsmBI* type-II restriction site using the protocol from ref. 2. Both PCR products were digested with *BsmBI*, *NdeI*, and *BamHI* (NEB) and, subsequently, ligated into an empty p11 vector that had been digested with *NdeI* and *BamHI* to generate p11-RavAΔLARA. All constructs were verified by sequencing.

**Protein Expression and Purification.** RavA and LdcI full-length proteins were purified as described earlier (1). RavAΔLARA was expressed and purified using the same protocol as that used for WT RavA. The LARA domain was expressed in BL21-gold (DE3) pLysS (Stratagene). The protein was then purified on Ni-NTA resin (Qiagen), a Mono S 5/50 GL cation exchange column (GE/Amersham), and then on a Superdex 75 10/300 (GE/Amersham) size exclusion chromatography column. Fractions were pooled, concentrated, and quantified using absorbance.

**RavA ATPase Activity.** ATP hydrolysis rates were measured as previously described using the malachite green assay (1). Reaction buffer contained 0.1 M Hepes, pH 7.5, 5 mM MgCl<sub>2</sub>, 0.02% Triton X100, 1 mM β-mercaptoethanol, 1 mM ATP, and 250 nM RavA at 37°C. The reaction was also carried out in the absence and presence of 100 μM of GTP, GDP, pppGpp, or ppGpp.

**Surface Plasmon Resonance (SPR) measurements.** To measure the binding affinities, SPR experiments were performed using BiacoreX instrument (GE Healthcare) at 25°C. The ligand (LdcI or RavA or RavAΔLARA) was attached to a Biacore sensorchip (CM5) by amine coupling using the Biacore amine coupling kit (GE Healthcare) following the manufacturer's protocols. LdcI was injected at 200 nM in 10 mM NaAc buffer at pH 3.5 over an activated surface, whereas RavA/RavAΔLARA was injected at 200 nM in 10 mM NaAc buffer at pH 5 over an activated surface. One flow cell was immobilized with the ligand, whereas the other was activated and deactivated without protein immobilization (reference flow cell). To remove the effect of nonspecific binding to the chip surface, the sensorgrams in the reference flow cell were subtracted from the corresponding sensorgrams in the ligand immobilized flow cell. Sensorgrams were recorded by injecting the analyte (RavA, RavAΔLARA, or LARA domain in the case of immobilized LdcI or the LARA domain in the case of immobilized RavA or RavAΔLARA) at 20 μL min<sup>-1</sup> flow rate in running buffer containing 10 mM Hepes, pH 7.5, 150 mM NaCl, 0.005% P20 surfactant, and 3 mM EDTA. The surface was regenerated between injections with a 1-min pulse of 2 M NaCl (or 2 M MgCl<sub>2</sub> if needed) in running buffer. The steady-state responses were plotted versus the corresponding analyte concentrations and the dissociation constants were derived by fitting the data to a Langmuir binding models by using BiaEvaluation 4.1 software (GE Healthcare).

**Measuring LdcI Enzyme Kinetics Using Isothermal Titration Calorimetry.** The effect of RavA on LdcI enzyme kinetics were investigated

using an isothermal titration calorimetry (ITC) approach (3). The assays were performed using a MicroCal VP-ITC calorimeter at 25°C with a stirring speed of 310 rpm and a buffer consisting of 100 mM sodium MES, pH 6.5, 1 mM tris(2-carboxyethyl)phosphine-HCl (TCEP-HCl), 1 mM ATP, 0.25 mM MgCl<sub>2</sub>, and 0.1 mM pyridoxal-5'-phosphate (PLP). Various combinations of substrates and protein were added at the following final concentrations: RavA—250 nM, RavAΔLARA—250 nM, LdcI—25 nM, ppGpp—50 μM, and L-lysine—1 mM. The order of addition of various combinations of proteins and small molecules is indicated in Fig. 4A–C. For each experiment, a single injection of 75 μL was made and the initial rates were calculated in ORIGIN 7.0 using ΔH<sub>apparent</sub> for L-lysine of −3,161 cal mol<sup>-1</sup>. The intrinsic ATPase activity of RavA under these conditions was insufficient to generate a significant heat change and was, therefore, not considered in the rate calculations.

**Sedimentation Velocity Analytical Ultracentrifugation.** Sedimentation velocity analytical ultracentrifugation experiments were carried out at the Ultracentrifugation Service Facility at the Department of Biochemistry, University of Toronto. RavA (18 μM) and LdcI (40 μM) were mixed in a buffer containing 25 mM Tris-HCl pH 8, 200 mM NaCl, 1 mM TCEP, and 0.1 mM PLP. The experiment was carried out using a Beckman Optima XL-A analytical ultracentrifuge with an An-60 Ti rotor spun at 15,000 rpm at 4°C. Data were analyzed using SEDNTERP (4) and SEDFIT (5).

**Pull-Down Experiments.** *Escherichia coli* DY330 strain, in which a Sequential Peptide Affinity (SPA) tag (6, 7) was fused to the 3' end of the endogenous *ravA* gene, was used for pull-down experiments. The strain (2 L) was grown for 24 h in Terrific Broth complemented with 0.2% glucose to induce LdcI at 30°C. Cells were resuspended in SPA binding buffer (25 mM Tris-HCl pH 8, 200 mM NaCl, 0.2 mM EDTA, 0.5 mM DTT, 10 mM MgCl<sub>2</sub>, 2 mM ATP, 0.1 mM PLP, and 10% glycerol) with the addition of 5 mg/mL of lysozyme and 0.5 mg/mL deoxyribonuclease I and lysed by sonication. The soluble fraction was incubated with the anti-FLAG M2 agarose beads (2 mL) for 6 h. After washing, the beads were incubated overnight in the presence of 500 μL of TEV protease at 2 mg/mL in 5 mL SPA binding buffer. The cleaved RavA-CBP (calmodulin binding peptide) was harvested from the supernatant after centrifugation. The RavA-LdcI complexes were analyzed by size exclusion chromatography using a Superose 6 column (GE Healthcare).

**Media Shift Assays.** A media shift assay was performed to test the in vivo effect of RavA on the inhibition of LdcI by ppGpp. Four *E. coli* strains were used: MG1655 Δ*cadBA*, MG1655 pST39-RavA & pT7-pol26 (WT + *ravA*), MG1655 pST39-RavAΔLARA & pT7-pol26 (WT + *ravA*ΔLARA) and MG1655 pST39-RavA (K52Q) & pT7-pol26 (WT + *ravA*(K52Q)). The latter three strains overexpress RavA, RavAΔLARA, and RavA(K52Q), respectively, under T7 promoter. The pST39 plasmid is described in ref. 8. The pT7-pol26 plasmid is required to express the T7 polymerase and is described in ref. 9. Five hundred milliliters of each of the three strains was grown at 37°C in 40 mM [3-(N-morpholino)propanesulfonic acid] - [2-(N-morpholino)ethanesulfonic acid] (MOPS-MES) defined rich media (10), pH 5, 1.32 mM K<sub>2</sub>HPO<sub>4</sub>, 1× ACGU (0.2 mM of each of Adenine, Cytosine, Guanine, and Uracil), 50 ng/mL of each of the 20 amino acids, 0.1% (wt/vol) D-glucose, and 30 mM lysine. After an OD<sub>600</sub> of 0.2 was reached, 1 mM IPTG was added to the cell cultures to induce the



docking precision, the variation of the correlation between the fit and the EM map upon rotation of the best fit around its principal axes of inertia is plotted in Fig. S2. Whereas the correlation between this ab initio fit and the EM map of the RavA hexamer is 74%, the HslU based model of hexameric RavA fitted into the EM density according to the same procedure gave a correlation of 72%. This model can be easily obtained from the ab initio fit by a combination of small rotations of the monomer and the correlation difference lies within the uncertainty limit. Furthermore, the fit to HslU hexamer has the major advantage of preserving biologically relevant contacts between monomers.

A comparison of RavA structure with available structures in the Protein Data Bank using the program DALI revealed significant similarity between the structure of RavA AAA+ domain and the equivalent domain in many AAA+ ATPases. However, only a handful of these AAA+ proteins were solved as hexamers. The closest hexameric structures are (from the highest to the lowest Z-score): (i) ZraR sigma54 activator, (ii) HslU, (iii) RUVB-like helicase, and (iv) p97. Using these four proteins as a template, a model for RavA hexamer was built. These different models of RavA hexamers showed clashes in their structure with the least

number of clashes obtained when using HslU and the ZraR sigma54 activator as templates. Also, the generated RavA hexameric model obtained using sigma54 activator, RUVB-like helicase, and p97 had a closed shape whereby the RavA legs were almost parallel to the z axis. This observation was in disagreement with the EM 3D reconstruction shown in Fig. 2B where RavA displays a more open conformation. The RavA model obtained using HslU as a template gave an open shape of the hexameric model and, hence, was in general agreement with the 3D EM model. Hence, the choice of HslU as a template to build the RavA hexameric model.

The fit of the hexameric RavA atomic model and of the crystal structure of LdcI into the EM density of RavA-LdcI complex that we previously published (1) was done in VEDA in the same way. The low resolution of the negative stain map of the RavA-LdcI complex results in a fit uncertainty of about 30 deg around the C6 symmetry axis of the RavA hexamer. Within this uncertainty, we favor the fit which places the LARA domain of RavA in the general vicinity of the ppGpp binding pocket of LdcI and thus corroborates the whole of our biochemical data.

- Snider J, et al. (2006) Formation of a distinctive complex between the inducible bacterial lysine decarboxylase and a novel AAA+ ATPase. *J Biol Chem* 281:1532–1546.
- Ko JK, Ma J (2005) A rapid and efficient PCR-based mutagenesis method applicable to cell physiology study. *Am J Physiol Cell Physiol* 288:C1273–1278.
- Todd MJ, Gomez J (2001) Enzyme kinetics determined using calorimetry: A general assay for enzyme activity? *Anal Biochem* 296:179–187.
- Laue TM, Shah BD, Ridgeway TM, Pelletier SL (1992) *Theory of Computer Aided Interpretation of Sedimentation Data* (Royal Society of Chemistry, Cambridge, England), pp 90–125.
- Schuck P (2000) Size-distribution analysis of macromolecules by sedimentation velocity ultracentrifugation and lamm equation modeling. *Biophys J* 78:1606–1619.
- Zeghouf M, et al. (2004) Sequential peptide affinity (SPA) system for the identification of mammalian and bacterial protein complexes. *J Proteome Res* 3:463–468.
- Babu M, et al. (2009) Sequential peptide affinity purification system for the systematic isolation and identification of protein complexes from *Escherichia coli*. *Methods Mol Biol* 564:373–400.
- Tan S (2001) A modular polycistronic expression system for overexpressing protein complexes in *Escherichia coli*. *Protein Expr Purif* 21:224–234.
- Mertens N, Remaut E, Fiers W (1995) Tight transcriptional control mechanism ensures stable high-level expression from T7 promoter-based expression plasmids. *Biotechnology (NY)* 13:175–179.
- Neidhardt FC, Bloch PL, Smith DF (1974) Culture medium for enterobacteria. *J Bacteriol* 119:736–747.
- Otwinowski Z, Minor W (1997) Processing of X-ray diffraction data collected in oscillation mode. *Methods Enzymol* 276:307–326.
- Fodje MN, et al. (2001) Interplay between an AAA module and an integrin I domain may regulate the function of magnesium chelatase. *J Mol Biol* 311:111–122.
- Sheldrick GM (2008) A short history of SHELX. *Acta Crystallogr A* 64:112–122.
- De La Fortelle E, Bricogne G (1997) Maximum-likelihood heavy-atom parameter refinement for multiple isomorphous replacement and multiwavelength anomalous diffraction methods. *Methods Enzymol* 276:472–494.
- Project-4 CC (1994) The CCP4 suite: Programs for protein crystallography. *Acta Crystallogr D* 50:760–763.
- Emsley P, Cowtan K (2004) Coot: Model-building tools for molecular graphics. *Acta Crystallogr D* 60:2126–2132.
- Murshudov GN, Vagin AA, Dodson EJ (1997) Refinement of macromolecular structures by the maximum-likelihood method. *Acta Crystallogr D* 53:240–255.
- Davis IW, et al. (2007) MolProbity: all-atom contacts and structure validation for proteins and nucleic acids. *Nucleic Acids Res* 35:W375–383.
- Ludtke SJ, Baldwin PR, Chiu W (1999) EMAN: Semiautomated software for high-resolution single-particle reconstructions. *J Struct Biol* 128:82–97.
- Mindell JA, Grigorieff N (2003) Accurate determination of local defocus and specimen tilt in electron microscopy. *J Struct Biol* 142:334–347.
- Heymann JB, Cardone G, Winkler DC, Steven AC (2008) Computational resources for cryo-electron tomography in Bsoft. *J Struct Biol* 161:232–242.
- van Heel M, Harauz G, Orlova EV, Schmidt R, Schatz M (1996) A new generation of the IMAGIC image processing system. *J Struct Biol* 116:17–24.
- Frank J, et al. (1996) SPIDER and WEB: Processing and visualization of images in 3D electron microscopy and related fields. *J Struct Biol* 116:190–199.
- Shaikh TR, et al. (2008) SPIDER image processing for single-particle reconstruction of biological macromolecules from electron micrographs. *Nat Protoc* 3:1941–1974.
- Navaza J, Lepault J, Rey FA, Alvarez-Rua C, Borge J (2002) On the fitting of model electron densities into EM reconstructions: a reciprocal-space formulation. *Acta Crystallogr D* 58:1820–1825.

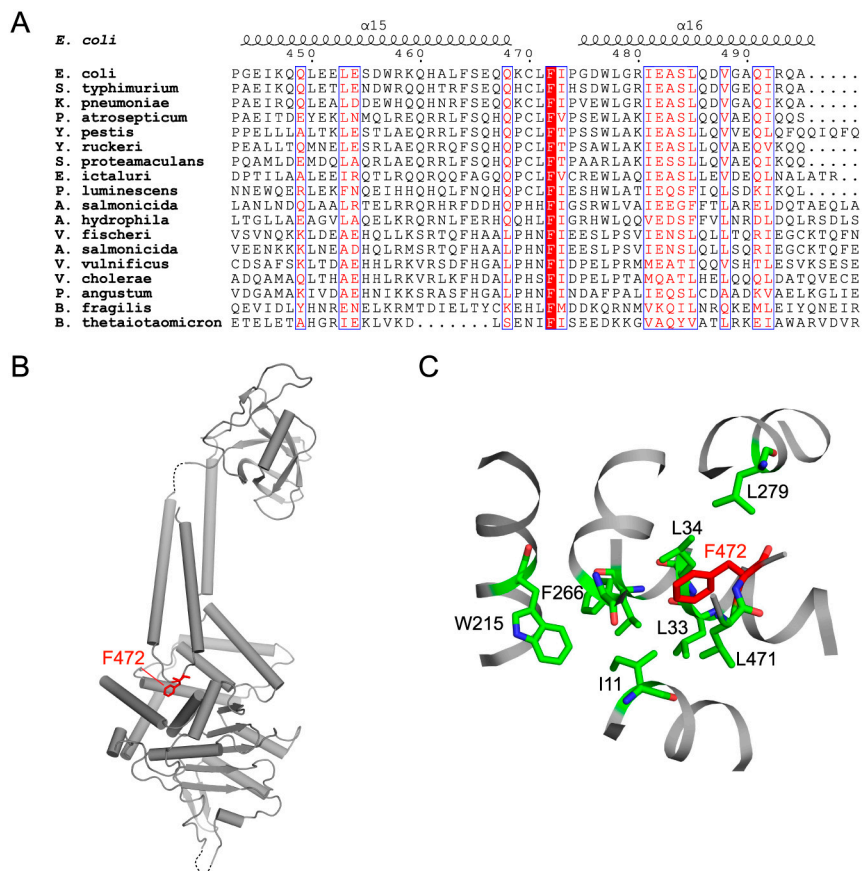


**Fig. S1.** F472 is an anchor point linking the C-terminal part of RavA with the AAA+ domain. (A) Sequence alignment of RavA helices  $\alpha 15$  and  $\alpha 16$  from some representative bacterial species showing the conservation of F472 residue. Sequences were aligned with ClustalW (1) and visualized with ESPript (2). (B) Ribbon diagram of RavA full-length protomer showing F472 residue in red located at the loop between helices  $\alpha 15$  and  $\alpha 16$ . (C) A close-up view of the hydrophobic pocket surrounding the F472 residue. The hydrophobic residues are shown in green.

1. Thompson JD, Higgins DG, Gibson TJ (1994) CLUSTAL W: Improving the sensitivity of progressive multiple sequence alignment through sequence weighting, position-specific gap penalties and weight matrix choice. *Nucleic Acids Res* 22:4673-4680.
2. Gouet P, Courcelle E, Stuart DI, Metz F (1999) ESPript: Analysis of multiple sequence alignments in PostScript. *Bioinformatics* 15:305-308.

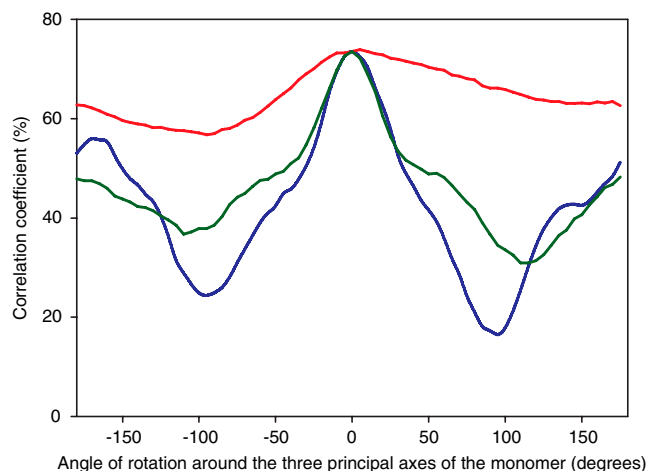


**Fig. S2.** Precision of docking the RavA monomer crystal structure into the RavA hexamer electron microscopy map. Correlation recorded as a function of the rotation angle around the inertia axes of the RavA monomer. Rotation around the x axis is shown in red, around the y axis in blue, and around the z axis in green.

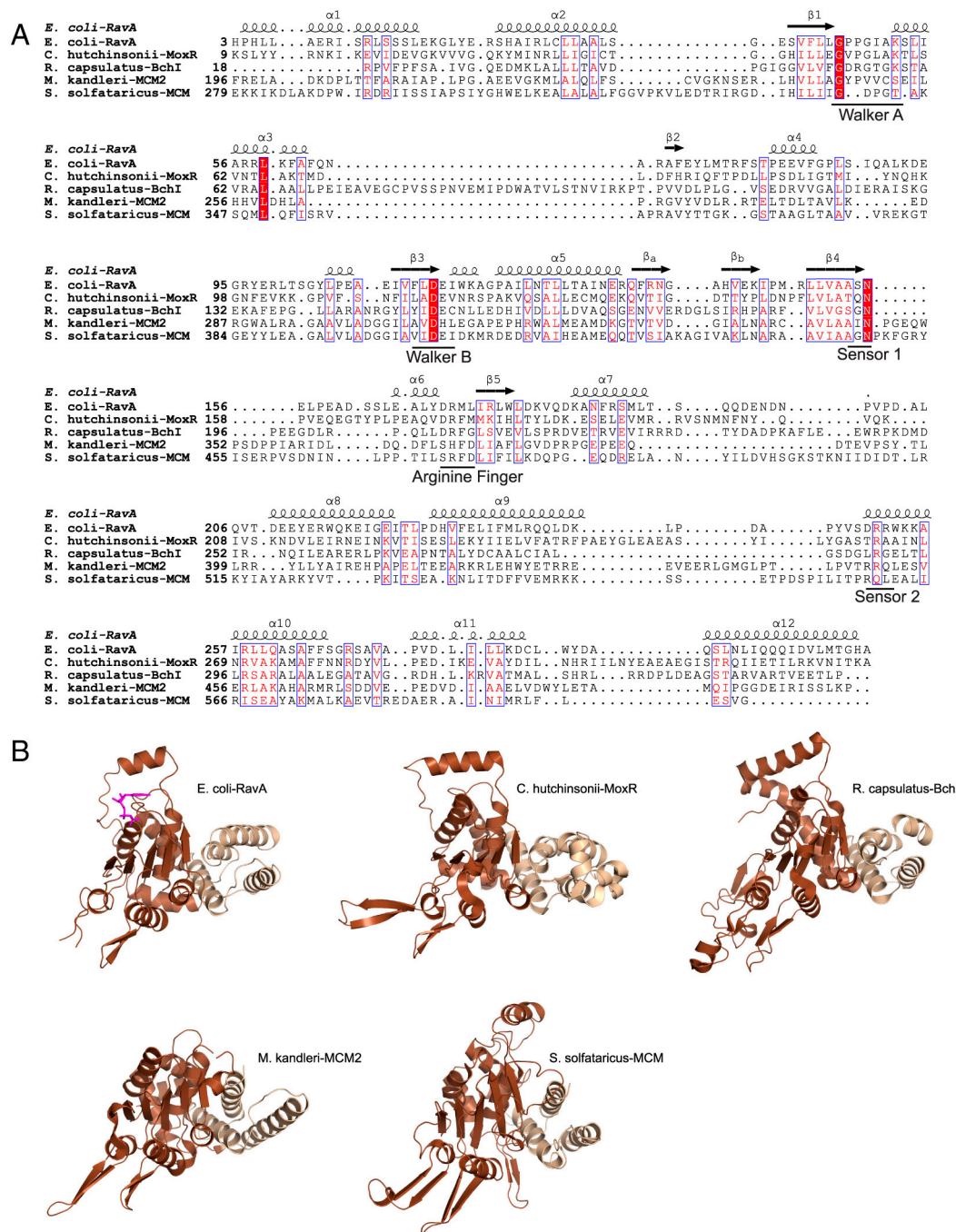


**Fig. S3.** RavA-like proteins. (A) Structure-based sequence alignment of *E. coli* RavA, the putative ATPase from *Cytophaga hutchinsonii* (PDB ID code 2R44), BchI subunit of *Rhodobacter capsulatus* Mg chelatase [PDB ID code 1G8P (1)], an archaeal MCM homolog from *Methanopyrus kandleri* [PDB entry 3F8T (2)], and archaeal minichromosome maintenance protein MCM from *Sulfolobus solfataricus* [PDB entry 3F9V (3)]. Structures were superposed using Dali (4), edited manually using SEAVIEW (5), and the sequence was visualized with ESPrnt (6). (B) Structures of the AAA+ domains of the above proteins. The  $\alpha\beta\alpha$  subdomain is colored in brown and the all- $\alpha$  subdomain in wheat.

1. Fodje MN, et al. (2001) Interplay between an AAA module and an integrin I domain may regulate the function of magnesium chelatase. *J Mol Biol* 311:111–122.
2. Bae B, et al. (2009) Insights into the architecture of the replicative helicase from the structure of an archaeal MCM homolog. *Structure* 17:211–222.
3. Brewster AS, et al. (2008) Crystal structure of a near-full-length archaeal MCM: Functional insights for an AAA+ hexameric helicase. *Proc Natl Acad Sci USA* 105:20191–20196.
4. Holm L, Kaariainen S, Rosenstrom P, Schenkel A (2008) Searching protein structure databases with DALI-Lite v.3. *Bioinformatics* 24:2780–2781.
5. Galtier N, Gouy M, Gautier C (1996) SEAVIEW and PHYLO\_WIN: Two graphic tools for sequence alignment and molecular phylogeny. *Comput Appl Biosci* 12:543–548.
6. Gouet P, Courcelle E, Stuart DI, Metoz F (1999) ESPrnt: Analysis of multiple sequence alignments in PostScript. *Bioinformatics* 15:305–308.

**A**

3.3 1.7 0.85 0.43 0.22

MW (MDa)

anti-Ldcl

anti-RavA

**B**

$\alpha(s)$  distribution ( $A_{280} S^{-1}$ )

Sedimentation Coefficient  $s_{20,w}$  (S)

peak	$s_{20,w}$ (S)	MW (MDa)	% of total
1	22.7	0.82	44.9
2	50.2	2.71	21.5
3	85.4	6.02	18.5

6 of 8

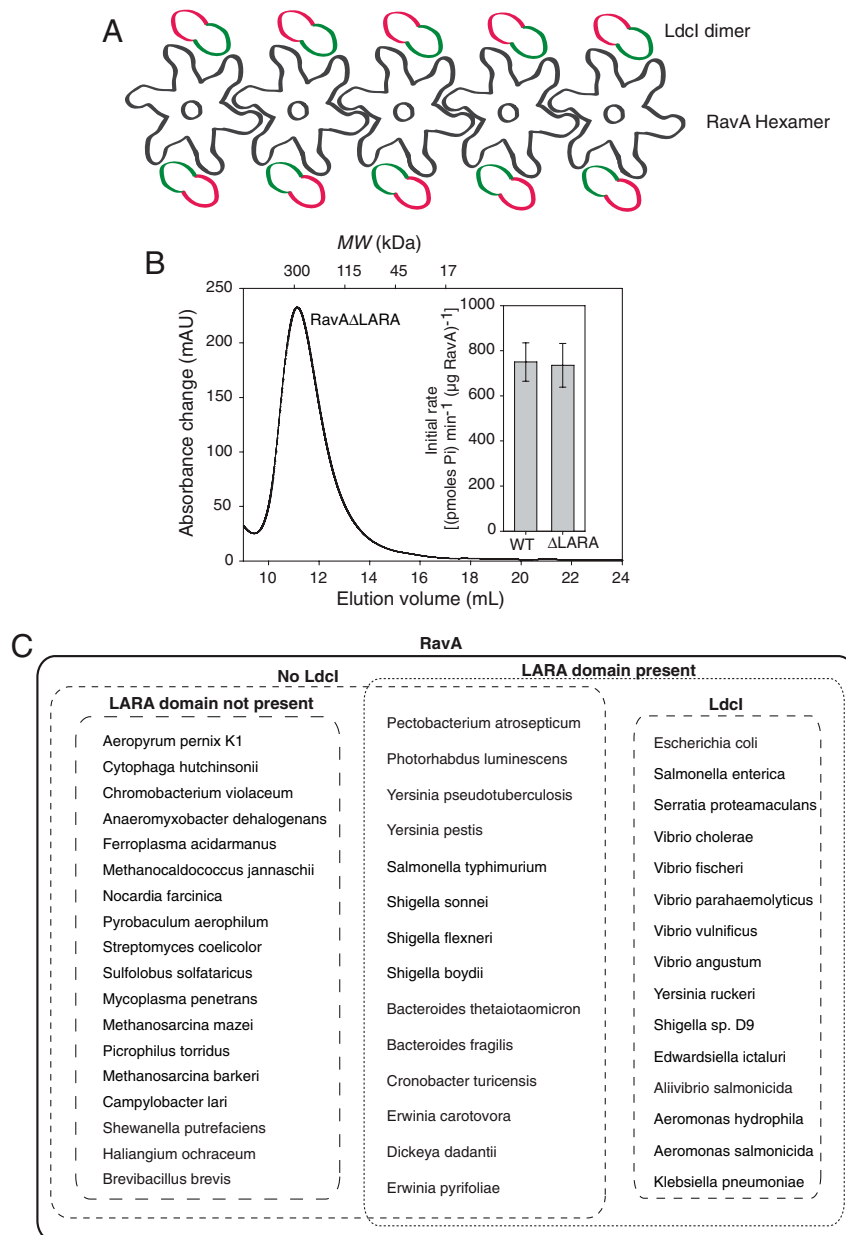


**Fig. S6.** The LARA domain is required for RavA-Ldcl and RavA-RavA interactions. (A) A schematic model illustrating RavA-Ldcl and RavA-RavA interactions within the RavA-Ldcl cage-like structure. (B) Size exclusion chromatography of RavA $\Delta\text{LARA}$  using Superdex 200 column in the presence of 1 mM ATP. Molecular weight standards are indicated on top. (Inset) The ATPase activity of RavA $\Delta\text{LARA}$  compared to that of WT RavA. (C) Venn diagram illustrating the bioinformatic analysis of 47 strains containing RavA for the presence of Ldcl and of the LARA domain in RavA.

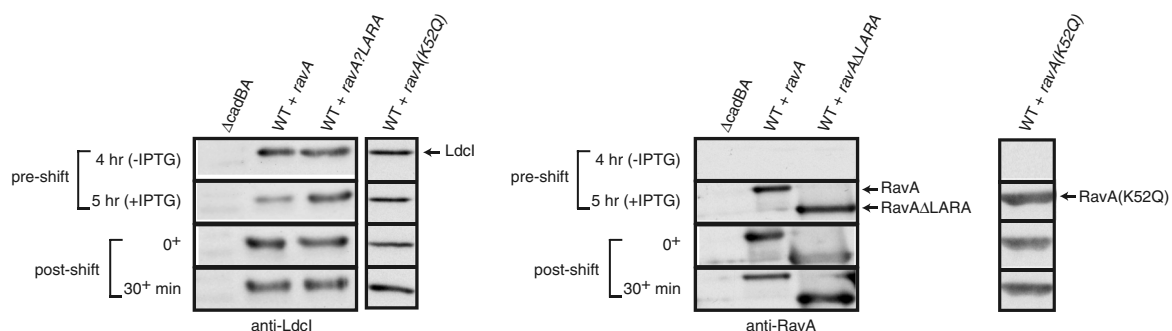


**Fig. S7.** Ldcl and RavA levels in the media shift assays of Fig. 4D. The levels of Ldcl, RavA, RavA $\Delta\text{LARA}$ , and RavA(K52Q) pre- and postshift were determined by Western blot analysis at the indicated time points in the media shift assays. The RavA(K52Q) gel was run separately from the other three. RavA is present after IPTG induction for all strains. Endogenous RavA is not expressed (or is at very low levels) in log phase cells.

Table S1. Crystallographic data collection and refinement statistics

	Native	EMTS derivative
<u>Data collection</u>		
Detector	ADSC Q315r	MAR 225
Space group	$P6_5$	$P6_5$
Unit cell a, b, c (Å)/ $\alpha$ , $\beta$ , $\gamma$ (°)	162.23, 162.23, 55.31/90.00, 90.00, 120.00	162.56, 162.56, 55.38/90.00, 90.00, 120.00
Wavelength (Å)	0.9393	1.004
Resolution (Å)	29.70–2.91 (3.04–2.91)	81.00–3.50 (3.70–3.50)
Observed reflections	92,591 (7,371)	160,100 (29,277)
Multiplicity	5.7 (3.4)	14.6 (14.8)
Completeness (%)	99.3 (95.6)	99.9 (99.8)
$R_{\text{merge}}$	0.065 (0.408)	0.088 (0.286)
$I/\sigma(I)$	25.0 (2.9)	10.9 (3.1)
Wilson plot B factor (Å <sup>2</sup> )	88	115
<u>SIRAS Phasing (SHARP)</u>		
Resolution range (Å)	47.60–3.50	
Number heavy atoms	5 Hg	
Phasing power (centric/acentric)	0.413/0.362	
$R_{\text{cullis}}$ (centric/acentric)	0.883/0.911	
<u>Refinement (REFMAC5)</u>		
$R_{\text{cryst}}$	0.230	
$R_{\text{free}}$	0.274	
Average B value (Å <sup>2</sup> )	75.0	
<u>Ramachandran plot (Molprobrity)</u>		
Favored regions	97.7%	
Additional allowed	2.3 %	
rms deviation bond/angles	0.006 Å/0.977°	

Values in parentheses refer to the highest resolution shell. The various crystallographic parameters are defined as follows:  $R_{\text{merge}}$ ,  $\sum |I_i - \langle I \rangle| / \sum I_i$ , where  $I_i$  is the intensity of the  $i$ th observation,  $\langle I \rangle$  is the mean intensity of the reflection, and the summation extends over all data;  $R_{\text{Cullis}}$ ,  $\sum |F_H - F_P| / \sum |F_{PH} - F_P|$ , where  $F_H$  is the calculated heavy atom structure factor contribution; phasing power,  $\langle F_H \rangle / \langle E \rangle$ , where  $E$  is the root mean square lack of closure;  $R_{\text{cryst}}$ ,  $\sum |F_{\text{obs}} - F_{\text{calc}}| / \sum F_{\text{obs}}$ , where  $F_{\text{obs}}$  and  $F_{\text{calc}}$  represent the observed and calculated structure factors, respectively.  $R_{\text{free}}$  was calculated using 5.2% of the observed reflections excluded from refinement. Excluded data were randomly selected.